# Wearable high-dielectric-constant polymer with core-shell liquid metal inclusions for biomechanical energy harvesting and self-powered user interface

| | |
|---|---|
| Journal: | *Journal of Materials Chemistry A* |
| Manuscript ID | TA-ART-01-2019-001249.R1 |
| Article Type: | Paper |
| Date Submitted by the Author: | 18-Feb-2019 |
| Complete List of Authors: | Gao, Shengjie; Purdue University, ; Purdue University <br> Wang, Ruoxing; Purdue University <br> Ma, Chenxiang; Purdue University, School of Industrial Engineering <br> Chen, Zihao; Purdue University <br> Wang, Yixiu; Purdue University, Industrail Engineering <br> Wu, Min; Purdue University, ; <br> Tang, Zhiyuan; Tianjin University <br> Bao, Ning; Nantong University, School of Publich Health <br> Ding, Dong; Idaho National Laboratory, Energy & Environment Science and Technology <br> Wu, Wenxuan; Shenzhen Broadthink Advanced Materials Technologies Co., Ltd. <br> Fan, Fengru; University of California, Santa Barbara <br> Wu, Wenzhuo; Purdue University, School of Industrial Engineering |
| | |

# Wearable high-dielectric-constant polymer with core-shell liquid metal inclusions for biomechanical energy harvesting and self-powered user interface

Shengjie Gao[1, 2], Ruoxing Wang[1, 2], Chenxiang Ma[1, 2, 3], Zihao Chen[4], Yixiu Wang[1, 2], Min Wu[1, 2], Zhiyuan Tang[3], Ning Bao[5], Dong Ding[6], Wenxuan Wu[7]*, Fengru Fan[8]*, Wenzhuo Wu[1, 2, 9, 10]*

[1]School of Industrial Engineering, Purdue University, West Lafayette, Indiana 47907, USA
[2]Flex Laboratory, Purdue University, West Lafayette, Indiana 47907, USA
[3]Department of Applied Chemistry, School of Chemical Engineering and Technology, Tianjin University, Tianjin, 300072, China
[4]School of Electrical and Computer Engineering, Purdue University, West Lafayette, Indiana 47907, USA
[5]School of Public Health, Nantong University, Nantong, Jiangsu, 226019, China
[6]Energy & Environment Science and Technology, Idaho National Laboratory, Idaho Falls, Idaho 83415, USA
[7]Shenzhen Broadthink Advanced Materials Technologies Co., Ltd., Shenzhen, Guangdong, 518117, China
[8]Department of Chemistry & Biochemistry, University of California, Santa Barbara, CA 93106, USA
[9]Birck Nanotechnology Center, Purdue University, West Lafayette, Indiana 47907, USA
[10]Regenstrief Center for Healthcare Engineering, Purdue University, West Lafayette, Indiana 47907, USA
*e-mail: Correspondence and requests for materials should be addressed to W. Z. W (wenzhuowu@purdue.edu), F. R. F (fengrufan@ucsb.edu), or W. X. W (wxwu@mail.ustc.edu.cn)

## Abstract

Deformable energy devices capable of efficiently scavenging the ubiquitous mechanical signals enables the realization of self-powered wearable electronic systems for emerging human-integrated technologies. Triboelectric nanogenerators (TENGs) utilizing soft polymers with embedded additives and engineered dielectric property emerge as ideal candidates for such applications. However, the use of solid filler materials in the state-of-the-art TENGs limit the devices' mechanical deformability and long-term durability. The current structural design for TENGs faces the dilemma where the enhanced dielectric constant of TENG's contact layer leads to an undesirable saturation of the surface charge density. Here, we present a novel scheme to address the above issues, by exploring a liquid-metal-inclusion based TENG (LMI-TENG) where the inherently deformable core-shell LMI are incorporated in the wearable high-dielectric-constant polymers. Through a holistic approach integrating theoretical and experimental efforts, we identified the parameter space for designing LMI-TENG with co-optimized output and mechanical deformability. As a proof of concept, we demonstrated LMI-TENG based wireless media control system for the self-powered user interface. The device architecture and design scheme presented here provides a promising solution towards the realization of self-powered human-integrated technologies.

## Introduction

The capability of functional devices to scavenge the environmental energy through sustainable pathways is expected to enable exciting opportunities in self-powered micro-/nano-systems for emerging technologies[1-5], e.g., pervasive computing, advanced healthcare, human-machine interface, robotics, and the Internet of Things (IoT). An assortment of technologies has been developed to transform the otherwise wasted ambient mechanical energy into electrical power through mechanisms such as electrostatic, piezoelectric, and recently, triboelectric processes. Triboelectric nanogenerators (TENG) can efficiently harvest the ubiquitous mechanical energy for powering electronics and sensors, hinged on principles of triboelectrification and electrostatic induction[6-10]. Ongoing TENG efforts primarily focus on augmenting power generation by increasing surface area, engineering the physical/chemical properties of contacting surfaces and implementing practical applications[11-13]. Among these efforts, increasing the surface charge density through engineering the charge-trapping capabilities of the dielectric layers has been shown effective in boosting the TENG performance [14-18]. Previous reports on such dielectric engineering suggest that the charge trapping ability of the contact layer (CL) in TENG increases with the increased dielectric constant of the polymer layer[14], leading to improved TENG performance. Nevertheless, the secondary-phase additive materials used for dielectric engineering in the state-of-the-art TENGs are exclusively solid type[14, 19, 20] with limited deformability. The inherently rigid nature of these materials results in a severe compliance mismatch with the soft elastomer and issues such as undesirable stress concentrations and layer delamination, leading to deteriorated bulk deformability and long-term durability for wearable and stretchable applications[21, 22]. Moreover, recent studies suggest the saturation of surface charge density in the CL could significantly limit TENG's performance[23]. Under such a condition, the widely adopted electrostatic models[24] fail to provide a fair evaluation of TENG performance and guidance for robust and optimal design.

To bridge these fundamental gaps and address the technological issues, here we present the design and implementation of a liquid-metal-inclusion based TENG (LMI-TENG) with desirable deformability and optimized performance. The incorporation of the deformable core-shell liquid metal/native oxide inclusions (Fig. 1a inset) in TENG's silicone layers (Fig. 1c) enables a synergistic engineering of the surface charge density at the material level, of the dielectric environment at the structure level, and of the boosted output power with desired deformability at the device level. Through a holistic integration of modeling and experiments, we demonstrate that the output performance of LMI-TENG can be enhanced by 250% with an optimized, constant surface charge density for the CL when 50 wt.% LMI is incorporated. We further reveal and identify for the first time the role of the surface leakage charge, a factor ignored by previous TENG studies, on the electrostatic process in LMI-TENG. With these new fundamental understandings, we present a proof-of-concept demonstration of the LMI-TENG based wireless media control system for future human-integrated applications, e.g., self-powered user interface[13, 25].

### The device structure of LMI-TENG

Figs. 1a and 1c show the optical image and 3D schematics of an LMI-TENG, which consists of a layer of liquid metal embedded functional silicone (LMEFS) sandwiched by two Ecoflex® layers (thickness of each layer ~100 μm). The LMI-TENG has an indium tin oxide (ITO) back electrode

(BE) and a grounded aluminum reference electrode (RE). LMEFS layer was prepared by mixing different weight fractions (wt.%) of Galinstan (a eutectic alloy with the composition ratio of Ga:68.5%, In:21.5%, and Tin:10%) liquid metal particles (LMPs) with the Ecoflex silicone through a mechanical stirring process (Supporting Fig. 1 and Methods). Galinstan has a native oxide skin (~ 1-3 nm thick) which conformably covers each liquid metal particle once being exposed to the air[26, 27]. The core-shell liquid metal/native oxide structures facilitate the homogeneous dispersion of LMPs and eliminate the formation of a continuous conductive path among LMPs in the LMEFS[28]. The two additional Ecoflex layers (Fig. 1c) ensure a constant surface charge density on the CL for LMI-TENGs with different wt.% LMPs under the same mechanical inputs (detailed discussions are included in the section 'Characterization of LMI-TENG's working performance'). This unique structural design in LMI-TENG, different from previous TENGs[29-31] where the CL's surface charge density changes with the various dielectric constants, is critical for avoiding the potential interference from the different surface charge densities due to the different LMP wt%, and helping develop a new fundamental understanding of the performance optimization in LMI-TENG through synergistically engineering both the dielectric property and the surface charge density. Fig. 1b shows a series of top-view optical images of the LMEFS layers containing different wt.% of LMPs. The post-processed images (see Methods) indicate that the shapes of the LMPs are ellipsoidal, with the primary radii ranging from 15 $\mu$m to 200 $\mu$m (Supporting Figs. 2 and 6c). The spatial distribution of LMPs within the LMEFS was visualized by the 3D micro-computed tomography (Micro-CT) images of the sandwiched dielectric stacks (SDS) (Supporting Fig. 2), showing a homogeneous dispersion of LMPs without forming a conductive percolation network, which is further confirmed by the dielectric measurement (Fig. 2c). If a percolation network exists, the dielectric constant of the SDS should decrease significantly[32], which is contrary to the result shown in Fig. 2c.

### Characterization of LMI-TENG's performance

We experimentally characterized the open-circuit voltage ($V_{oc}$), short-circuit current density ($J_{sc}$) and short-circuit transferred charge density ($\sigma_{sc}$) when different wt.% LMP was mixed into the LMEFS. The result (Fig. 2a (i)) shows that a 250% enhancement can be achieved in $V_{oc}$ when the LMP concentration is increased from 0 wt.% to 50 wt.%. A similar enhancement is also observed for $J_{sc}$ and $\sigma_{sc}$ (Figs.2a (ii)-(iii)). When the concentration of LMP is further increased (e.g., from 50 wt.% to 70 wt.%), the output performance starts to degrade (Fig. 2b), though the absolute values of $V_{oc}$, $J_{sc,}$ and $\sigma_{sc}$ are still more than twice greater than those obtained for the pristine TENGs without LMI. Supporting Fig. 3a shows that the output power of 50 wt.% LMI-TENG reaches 13.95 mW/m$^2$, suggesting its potential to meet the power requirement for driving the operation of IoT devices[3]. The ideal cycles of maximized energy output (CMEO)[33], a standard method to characterize the ideal maximum output performance of TENG, for the LMI-TENG with different LMP wt.% are compared in Supporting Fig. 3b, showing that LMI-TENG can deliver a maximum output energy density of 1.33mJ/m$^2$ per cycle. Dielectric measurements for different SDSs ($\varepsilon_{SDS}$) (Fig. 2c) are consistent with the electrical characterization result. When the LMP wt% increases from 0 wt% to 50 wt%, $\varepsilon_{SDS}$ increases from 4.58 to 12.65, and starts to drop when the LMP wt% further increases to 70 wt%. The constant surface charge density for LMI-TENGs with different LMP wt.% was confirmed by the Kelvin Probe Force Microscope (KPFM) characterization (see Methods). For each device, the surface potentials for both the aluminum electrode and the

CL are measured (Fig.2d and Supporting Fig.4), showing no significant difference in the surface potential for CLs from different LMI-TENGs, indicating that the densities of surface charges on each CL remain constant as per our expectation[34]. The constant surface charge density of CL (Fig. 2d) is supposed to lead to a constant TENG output based on the previous theoretical report[24]. However, LMI-TENG's working performance varies with the different weight fraction of LMP (Fig. 2b), indicating that a deeper understanding of the working mechanism of TENG is necessary.

**Dielectric engineering and analysis of SDS**

To better understand the relationship between the LMP wt.% and the dielectric constant of SDS for revealing the operation mechanism of LMI-TENG, we apply the percolation theory to quantitatively analyze the dependence of $\varepsilon_{SDS}$ on the LMP wt.%. Given that the SDS can be considered as a binary-phase system, where Ecoflex silicone is the matrix material and LMPs are the secondary-phase additives, the effect of LMP concentration on such a composite system's general physical properties can be expressed as[32],

$$Properties \propto (f_c - f_i)^{-s\prime} \qquad (1)$$

where $f_i$ is the relative fraction of the secondary phase, $f_c$ is the percolation threshold related to the disappearance of the long-range, global connectivity of the second phase in the matrix, and s' is the critical exponent used to characterize the percolation transition[35]. When considering the dielectric property, this relationship can be adapted into[36],

$$\varepsilon = \varepsilon_0 \left[\frac{f_c - f}{f_c}\right]^{-s\prime} \qquad (2)$$

where $\varepsilon_0$ is the initial dielectric constant of the pristine Ecoflex, $f$ is the weight fraction of the second phase, and $f_c$ is the corresponding percolation threshold. The solid red curve in Fig. 2c shows the fitting result using equation (2), with the fitted values of $f_c$ for LMEFS is 0.7 and the corresponding $s'$ is 0.865. The derived value for $s'$ falls within the reasonable range (0.8~1) for a binary system[37]. Therefore, according to the definition of the percolation threshold, $\varepsilon_{SDS}$ should reach the maximum when the LMP wt.% is 70%. This is, however, contradictory to the experimental results shown in Fig. 2b and Fig. 2c which indicate an actual percolation threshold value at ~ 50%. Such a discrepancy can be understood as follows.

It is known that the dielectric constant of a binary system is closely related to the geometrical factor and the spatial distribution of the second-phase additives[32]. We run the selected area particle analysis on LMEFS (see Methods), and the statistical result shown in Supporting Fig.6b suggests a positive correlation between the LMP wt.% and the percentage of the projected area occupied by LMPs inside the silicone matrix. However, when the LMP concentration increases from 50% to 70%, there is no significant change on the percentage of the projected occupied area, indicating that the spatial distribution of LMPs should not be the main factor affecting the dielectric property of the SDS. Furthermore, $\varepsilon_{SDS}$ shows a frequency-independent characteristic (Supporting Fig. 5a), suggesting that the microcapacitor-structure model (MSM)[32, 38-40] widely adopted for the near-percolation-threshold dielectric constant could be applied to understand the effect of LMPs' geometrical factor on $\varepsilon_{SDS}$. Within a certain range (from 5 wt.% to 50 wt.%), the increased wt.% of LMP leads to the dispersion of more LMPs and a decreasing distance (Supporting Figs. 6a and c) between adjacent LMPs. According to the MSM theory[40], such changes

4

lead to a higher $\varepsilon_r$. When the LMP concentration reaches 70 wt.%, the amount of LMPs is expected to continue increasing, and the distance between the adjacent LMPs should decrease further. However, the centrifugal force induced in the fabrication and the mechanical pressing[26] from CE during the contact-separation TENG process is likely to lead to the fusion of smaller LMPs into larger LMPs. This fusion process is confirmed in Supporting Fig. 6b which shows that the number of LMPs decreases by 40% while the LMP concentration increases from 50 wt.% to 70 wt.%. Moreover, the statistical result of the primary radius distribution for different LMEFS (Supporting Fig. 6d) suggests that LMPs with larger primary radius (>250μm) only appear in LMEFS with 70 wt.% LMP. Thus, even though the distance between the adjacent LMPs does not vary significantly (Supporting Fig. 6c), the reduced amount of LMPS inside the Ecoflex matrix leads to a smaller $\varepsilon_{SDS}$. Finally, the measured dissipation factor (D), which evaluates the dielectric material's capability to store charge, for SDS (50 wt.% LMP) is smaller than that for the pristine Ecoflex matrix in the low-frequency range (Supporting Fig. 5b), similar to the previous reports[28]. This observation is in sharp contrast to the previous reports for other known high-*k* polymers[41], which generally show an increased dissipation factor when the dielectric constant increases[42]. Our result suggests that LMEFS could be a promising candidate for future applications such as energy storage devices and smart skins[43] where both high-*k* and low dissipation factor are needed[20].

**The operation mechanism of LMI-TENG and the role of surface leakage charge**

To bridge the gap between the KPFM data and TENG output performance, we further studied the electrostatic induction within the SDS and BE. The effect of this electrostatic induction on the TENG performance has been ignored in previous studies under the ideal open circuit condition[14, 44]. The general expression for the TENG output voltage is[44]:

$$V = \frac{\sigma x(t)}{\varepsilon_0} - \frac{Q}{S\varepsilon_0}\left(x(t) + \frac{d_{SDS}}{\varepsilon_{SDS}}\right) \tag{3}$$

where σ is the triboelectric charge density on the CL surface, Q is the number of transferred charges between BE and RE, $d_{SDS}$ and $\varepsilon_{SDS}$ represent the thickness and dielectric constant of SDS, respectively. S is the contact area, x(t) is the time-dependent gap distance between the top surface of CL and RE, and $\varepsilon_0$ is the vacuum dielectric constant. Previous models assume that there is no charge transfer between BE and RE (Q=0) under open-circuit condition[24], and the ideal $V_{oc}$ is hence given by:

$$V_{oc} = \frac{\sigma x(t)}{\varepsilon_0} \tag{4}$$

Such an ideal model leads to a trivial electrical field inside the SDS[24] and the widely-accepted understanding that the effective way to boost $V_{oc}$ is to increase the surface charge density through approaches such as modulating the surface roughness of the CL, increasing the dielectric constant of SDS and etc[18, 29]. However, in reality, TENG has a finite dimension, and the electrical field originating from RE will not terminate at the air-CL interface as assumed in the previous models[44]. Therefore, there should be negative induction charges accumulated in BE due to the penetration of the electrical field ($E_{air}$) through SDS, where $E_{air}$ is between RE and the top surface of SDS. $E_{air}$ thus gives rise to the formation of a nontrivial electrical field ($E'_{SDS}$) which has the opposite direction to $E_{air}$ (Fig. 3a). As a result, the hypothetical condition Q=0 is not satisfied,

suggesting that a more practical model considering the electrostatic induction in the dielectric layer should be adopted[45]. Here, we present an analysis for our proposed model considering the LMEFS-dependent non-trivial electrical field within the SDS ($E'_{SDS}$). The modified effective electrical field ($E'$), which determines $V_{oc}$, in the TENG under the open-circuit condition should therefore be:

$$E' = \frac{1}{S \cdot \varepsilon_0}(\sigma S - \frac{Q'}{\varepsilon_{SDS}}) \tag{5}$$

where $Q'$ is the induced charge in BE (Fig.3a) by the propagating $E_{air}$ through the SDS. Consequently, $Q'$ can be considered as the "surface leakage charge" during the TENG operation. To our best knowledge, the role of such surface leakage charge has not been studied in previous experimental studies.

According to equation (5), if the dielectric constant of SDS ($\varepsilon_{SDS}$) increases, $E'$ will also increase, leading to a boosted $V_{oc}$. If $\varepsilon_{SDS}$ is infinite, $E'$ will be equal to $\sigma/\varepsilon_0$, same to the case for the infinitely large parallel plate capacitor, which is the fundamental model in the previous TENG work[44]. Finite Element Analysis (FEA) was carried out by using COMSOL Multiphysics to further verify the correlation between the dielectric constant of SDS and $E'_{SDS}$. As shown in Fig. 3b, $E'_{SDS}$ decreases when $\varepsilon_{SDS}$ increases, leading to an increased $E'$. Consequently, the modified expression for the true open-circuit voltage of TENG should be:

$$V_{oc,true} = \frac{\sigma x(t)}{\varepsilon_0} - \frac{Q'}{S \varepsilon_0}(x(t) + \frac{d_{SDS}}{\varepsilon_{SDS}}) \tag{6}$$

We now turn to the discussion for the short-circuit condition when $Q'$ is included in the model. If the amount of the total transferred charges without $Q'$ is $Q_{tr}$, the real transferred charges should be $Q_{tr}-Q'$. Therefore, the output power, which is closely related to the amount of transferred charges between the two electrodes, will decrease accordingly. It should be noted that the magnitude of $Q'$ depends on many factors[24]. In our experiment, $\varepsilon_{SDS}$ is the main contributor since other factors such as the thickness of SDS is controlled through the device fabrication. With the increased $\varepsilon_{SDS}$, $E'_{SDS}$ will be largely confined within the SDS, which decreases $Q'$ and results in a higher $I_{sc}$ and $Q_{sc}$. Since the existence of $Q'$ can significantly affect the TENG performance, more efforts are warranted for a comprehensive evaluation of $Q'$ in the future work.

The modified working mechanism for LMI-TENG can then be understood using the illustrations in Fig. 3c. When the aluminum electrode contacts the CL of SDS, electrons tend to be transferred from the aluminum RE to the CL[46], leaving aluminum positively charged while the top surface of CL negatively charged[21] (Fig. 3c (i)). Once the two surfaces separate from each other, an electrical field will be established due to the separation of positive and negative charges, driving the flow of electrons from the ITO BE to the ground (Fig. 3c (ii)). In the meantime, the leakage charge within the BE (Fig. 3c (i)) due to the imperfect screening will dampen the electron transfer and thus affect the $V_{oc}$ (Fig. 3c (ii)). With the increased distance between the aluminum and the CL, the resultant open-circuit voltage ($V_{oc}$), short-circuit current density ($J_{sc}$), and density of transferred charge between the two electrodes ($\sigma_{sc}$) all increase monotonically until a maximum gap distance is reached[24](Fig.3c (iii)). Subsequently, when the aluminum electrode moves towards the CL, the established electrical field within the LMI-TENG will decrease (Fig.3c (iv)), resulting in the flow of electrons back to the BE to reach an electrostatic equilibrium[9].

### Prototypical demonstration of a self-powered user interface

We further designed and demonstrated a stretchable LMI-TENG device, with spray-coated silver nanowires (see Supporting Fig. 7 and Methods) as the BE. The incorporation of sliver-nanowire electrodes significantly improves the mechanical stretchability and stability of the LMI-TENG, with no significant degradation in both the electrode conductivity and device output performance after 4500-cycle of the stretch-release test (a maximum strain of 100%) (Fig. 4a). Compared to the LMI-TENG devices with 0 wt.% LMP, the output performance of LMI-TENG with 50 wt.% LMP is boosted with an enhancement of 300% (Supporting Figs. 8a-c), consistent with the results shown in Fig. 2c when ITO electrodes are used. More significantly, the stretchable LMI-TENG shows great potential to efficiently harvest mechanical energy at a low frequency (e.g., 0.8 Hz)[47,48,49, 50], which is important for human-integrated applications as well as harvesting larger-scale mechanical energy, e.g., ocean wave[51].

The feasibility of our wearable LMI-TENG for potential application in human-integrated technology, e.g., user interface[13, 25], has been explored. We demonstrated a stretchable LMI-TENG based wireless media control system (MCS) (Fig. 4b and Supporting Fig. 9a). The device can adhere to the human skin conformably without using a tape (Fig. 4b). The high stretchability of Ecoflex silicone and sliver-nanowire BE ensures that our device can withstand various types of deformation caused by the finger/skin motion during the daily operation. The LMI-TENG possesses a good sensitivity in the low-pressure region (Supporting Fig. 9b), promising for human motion detection[25, 52]. Our prototypical device consists of three digitized LMI-TENG unit (#0, #1, #2), and the data acquisition interface is realized using a 10-bit analog-to-digital converter (ADC) (Supporting Fig. 9c and Methods). The adoption of serial communication enables the monitoring of the MCS working status (Supporting Fig. 9d). Our LMI-TENG MCS is capable of detecting and encoding different finger motions into electrical signals with distinct patterns for wirelessly controlling a music player on a remote computer (Supporting Fig. 9a ). Fig.4c shows the electrical outputs from the three LMI-TENGs in MCS when the "Play/Pause" function is initiated by only touching the unit #0. The setting of detection threshold ($V_{th}$)can address the issue of signal interference in a micro-controller unit (MCU)[12] by utilizing different logic level in each unit. Our MCS can detect the finger motion by identifying the change of the logic level combination of each three pins in MCU. When the sequence of logic level is switched from "0, 0, 0" to "0, 1, 0" to "0, 0, 1", indicating that the finger is sliding from LMI-TENG #2 to #3 (Supporting Video), the system volume will be increased. When the sequence of logic level is switched from "0, 0, 0" to "0, 0, 1" to "0, 1, 0", the MCS will decrease the system volume (Supporting Video). The electrical signal processed by the MCU is shown in Fig. 4d. Our system provides a controllable and versatile platform for designing and implementing LMI-TENG based wearable device in various societally-pervasive applications including human-machine interface, remote operation, and smart artificial skin.

### Conclusion

In conclusion, we present a platform for exploring liquid-metal-inclusion based TENG where the deformable core-shell liquid metal inclusions are incorporated in the wearable high-dielectric-constant polymers. Our structural design enables the co-optimization for the dielectric engineering and the surface charge density engineering. Through a holistic integration of

modeling and experiments, we identify the design parameters space for enabling LMI-TENG with optimized output and mechanical deformability. The role of the surface leakage charge, a factor ignored by previous TENG studies, has been theoretically and experimentally investigated for the first time, which extends the theoretical framework of TENG and advances the fundamental understanding of TENG's design and optimization. The device architecture and design scheme shown here provides a promising solution for optimizing both the TENG devices' wearability and operation performance through cost-effective, scalable approaches. Our work presents an important step towards the realization of self-powered human-integrated technologies.

**Author contributions** W. Z. W. and S. J. G conceived the idea. W. Z. W. designed the experiments and supervised the project. W. Z. W. and S. J. G. analyzed the data and wrote the manuscript. S. J. G. fabricated the LMI-TENG devices and performed the characterizations. S. J. G. carried out the FEA simulations. F.R.F. synthesized the silver nanowires and guided the experiments for stretchable electrodes. W. X. W. guided the experiments for LMI engineering. S. J. G. and Z. H. C. performed the prototypical demonstration. R. X. W., C. X. M., Y. X. W., and M. W. provided necessary help during the experiment. All authors have discussed the results and commented on the paper.

**Competing financial interest:** The authors declare no competing financial interests.

## Methods

**Fabrication of LMEFS.** A layer of Ecoflex 00-30 (1:1 Base & Cure by weight ratio and degassed for 10 minutes) was first coated onto the PET-ITO substrate using a spinner and cured on a hotplate under 60 °C. Then liquid Ecoflex base was mixed and mechanically stirred with liquid metal (Consolidated Chemical & Solvents) transferred by pipette for 7 minutes. After this, the composite was mixed with Ecoflex cure (1:1 by volume ratio), degassed for 10 minutes and cured under 60 °C. Finally, another layer of Ecoflex was again coated onto the previous layer and cured for another 10 minutes under 60 ° C.

**Fabrication of LMI-TENG.** For PET-ITO as the back electrode, after the fabrication of LMEFS, a copper wire was inserted on the back of the ITO as the conductive wire connected to the electrical measurement system. For silver nanowires (Ag NWs) as the back electrode, before the fabrication of LMEFS, a layer of Ag NWs was drop-casted onto the non-conductive PET side and annealed under 60 °C for 30 minutes. After the annealing, the following steps are the same as steps in the fabrication of LMEFS. After that, the whole device was peeled off from the PET substrate, a copper tape serving as the conductive wire was connected to the Ag NWs, and another layer of Ecoflex was blade coated over it.

**Particles Characterization.** The optical image was taken by Olympus BX53M and post-processed by ImageJ. (1) Each raw optical image was converted to a binary image (Image → Adjust → Threshold, with a lower cutoff of ≈15 and an upper cutoff of ≈230 and Dark background option); (2) each resulting binary image was segmented using the built-in ImageJ watershed routine (Process → Binary → Watershed); (3) the sizes for all segmented particles were obtained using ImageJ's particle analysis package (Analyze → Analyze Particles, with size range going from 10 square pixel units to infinity, circularity from 0 to 1, showing bare outline of particles); (4) the diameter for each particle was computed from the area output by ImageJ under a spherical approximation. The 3D spatial distribution of LMPs insides the Ecoflex matrix was carried out by The Scanco MicroCT u40 and the 3D image was constructed by MeshLab 2016.

**TENG Characterization and measurement.** The output performance of LMI-TENG was characterized by SR 570 (Stanford Research Systems) and Keithley 6514 electrometer. The KPFM was performed by using Keysight 5500 AFM under KPFM-AM mode. The dielectric constant was measured by using Keysight B1500A semiconductor device parameter under Capacitance-Frequency mode. The data communication between the LMI-TENG sensing unit, Bluetooth module (Adafruit) and the computer was performed via serial communication from an embedded computing platform (Arduino Uno, Arduino).

## References

1. Z. L. Wang and W. Wu, *Angewandte Chemie-International Edition*, 2012, **51**, 11700-11721.
2. Q. Zheng, Y. Zou, Y. Zhang, Z. Liu, B. Shi, X. Wang, Y. Jin, H. Ouyang, Z. Li and Z. L. Wang, *Science advances*, 2016, **2**, e1501478.
3. L. Atzori, A. Iera and G. Morabito, *Computer networks*, 2010, **54**, 2787-2805.
4. J. A. Rogers, T. Someya and Y. Huang, *science*, 2010, **327**, 1603-1607.
5. W. Gao, S. Emaminejad, H. Y. Y. Nyein, S. Challa, K. Chen, A. Peck, H. M. Fahad, H. Ota, H. Shiraki and D. Kiriya, *Nature*, 2016, **529**, 509.
6. Z. L. Wang, *Materials Today*, 2017, **20**, 74-82.
7. F.-R. Fan, Z.-Q. Tian and Z. Lin Wang, *Nano Energy*, 2012, **1**, 328-334.
8. Y. Zi, J. Wang, S. Wang, S. Li, Z. Wen, H. Guo and Z. L. Wang, *Nature Communications*, 2016, **7**, 10987.
9. Z. L. Wang, *ACS nano*, 2013, **7**, 9533-9557.
10. F.-R. Fan, L. Lin, G. Zhu, W. Wu, R. Zhang and Z. L. Wang, *Nano Letters*, 2012, **12**, 3109-3114.
11. S. Wang, L. Lin and Z. L. Wang, *Nano Energy*, 2015, **11**, 436-462.
12. J. Chen, G. Zhu, J. Yang, Q. Jing, P. Bai, W. Yang, X. Qi, Y. Su and Z. L. Wang, *ACS nano*, 2015, **9**, 105-116.
13. C. Wu, W. Ding, R. Liu, J. Wang, A. C. Wang, J. Wang, S. Li, Y. Zi and Z. L. Wang, *Materials Today*, 2018.
14. W. Seung, H. J. Yoon, T. Y. Kim, H. Ryu, J. Kim, J. H. Lee, J. H. Lee, S. Kim, Y. K. Park and Y. J. Park, *Advanced Energy Materials*, 2016.
15. J. Chen, H. Guo, X. He, G. Liu, Y. Xi, H. Shi and C. Hu, *ACS applied materials & interfaces*, 2015, **8**, 736-744.
16. Y. Yu, Z. Li, Y. Wang, S. Gong and X. Wang, *Advanced Materials*, 2015, **27**, 4938-4944.
17. S. Wang, Y. Xie, S. Niu, L. Lin, C. Liu, Y. S. Zhou and Z. L. Wang, *Advanced Materials*, 2014, **26**, 6720-6728.
18. N. Cui, L. Gu, Y. Lei, J. Liu, Y. Qin, X. Ma, Y. Hao and Z. L. Wang, *ACS nano*, 2016, **10**, 6131-6138.
19. J. Chun, J. W. Kim, W.-s. Jung, C.-Y. Kang, S.-W. Kim, Z. L. Wang and J. M. Baik, *Energy & Environmental Science*, 2015, **8**, 3006-3012.
20. J. Lu and C. Wong, *IEEE Transactions on Dielectrics and Electrical Insulation*, 2008, **15**.
21. Y. C. Lai, J. Deng, S. Niu, W. Peng, C. Wu, R. Liu, Z. Wen and Z. L. Wang, *Advanced Materials*, 2016, **28**, 10024-10032.
22. J. Wang, S. Li, F. Yi, Y. Zi, J. Lin, X. Wang, Y. Xu and Z. L. Wang, *Nature communications*, 2016, **7**, 12744.
23. J. Wang, C. Wu, Y. Dai, Z. Zhao, A. Wang, T. Zhang and Z. L. Wang, *Nature communications*, 2017, **8**, 88.
24. S. Niu, S. Wang, L. Lin, Y. Liu, Y. S. Zhou, Y. Hu and Z. L. Wang, *Energy & Environmental Science*, 2013, **6**, 3576-3583.
25. X. Pu, H. Guo, J. Chen, X. Wang, Y. Xi, C. Hu and Z. L. Wang, *Science advances*, 2017, **3**, e1700694.
26. J. W. Boley, E. L. White and R. K. Kramer, *Advanced Materials*, 2015, **27**, 2355-2360.
27. M. D. Dickey, R. C. Chiechi, R. J. Larsen, E. A. Weiss, D. A. Weitz and G. M. Whitesides, *Advanced Functional Materials*, 2008, **18**, 1097-1104.
28. M. D. Bartlett, A. Fassler, N. Kazem, E. J. Markvicka, P. Mandal and C. Majidi, *Advanced Materials*, 2016, **28**, 3726-3731.
29. Z. L. Wang, J. Chen and L. Lin, *Energy & Environmental Science*, 2015, **8**, 2250-2282.
30. Z. Fang, K. H. Chan, X. Lu, C. F. Tan and G. W. Ho, *Journal of Materials Chemistry A*, 2018, **6**, 52-57.

31. S. Cheon, H. Kang, H. Kim, Y. Son, J. Y. Lee, H. J. Shin, S. W. Kim and J. H. Cho, *Advanced Functional Materials*, 2018, **28**.
32. C.-W. Nan, Y. Shen and J. Ma, *Annual Review of Materials Research*, 2010, **40**, 131-151.
33. Y. Zi, S. Niu, J. Wang, Z. Wen, W. Tang and Z. L. Wang, *Nature communications*, 2015, **6**.
34. W. Melitz, J. Shen, A. C. Kummel and S. Lee, *Surface Science Reports*, 2011, **66**, 1-27.
35. L. Flandin, T. Prasse, R. Schueler, K. Schulte, W. Bauhofer and J.-Y. Cavaille, *Physical Review B*, 1999, **59**, 14349.
36. C. C. Wang, J. F. Song, H. M. Bao, Q. D. Shen and C. Z. Yang, *Advanced Functional Materials*, 2008, **18**, 1299-1306.
37. L. Wang and Z.-M. Dang, *Applied physics letters*, 2005, **87**, 042903.
38. X. Zeng, L. Deng, Y. Yao, R. Sun, J. Xu and C.-P. Wong, *Journal of Materials Chemistry C*, 2016, **4**, 6037-6044.
39. R. Simoes, J. Silva, R. Vaia, V. Sencadas, P. Costa, J. Gomes and S. Lanceros-Méndez, *Nanotechnology*, 2008, **20**, 035703.
40. C. Pecharromán and J. S. Moya, *Advanced Materials*, 2000, **12**, 294-297.
41. Z.-M. Dang, J.-K. Yuan, J.-W. Zha, T. Zhou, S.-T. Li and G.-H. Hu, *Progress in Materials Science*, 2012, **57**, 660-723.
42. J. Lu, K.-S. Moon, J. Xu and C. Wong, *Journal of Materials Chemistry*, 2006, **16**, 1543-1548.
43. L. Zhu, *The journal of physical chemistry letters*, 2014, **5**, 3677-3687.
44. S. Niu and Z. L. Wang, *Nano Energy*, 2015, **14**, 161-192.
45. R. D. I. G. Dharmasena, K. Jayawardena, C. Mills, J. Deane, J. Anguita, R. Dorey and S. Silva, *Energy & Environmental Science*, 2017, **10**, 1801-1811.
46. C. Xu, Y. Zi, A. C. Wang, H. Zou, Y. Dai, X. He, P. Wang, Y. C. Wang, P. Feng and D. Li, *Advanced Materials*, 2018.
47. Y. Zi, H. Guo, Z. Wen, M.-H. Yeh, C. Hu and Z. L. Wang, *Acs Nano*, 2016, **10**, 4797-4805.
48. F. Xing, Y. Jie, X. Cao, T. Li and N. Wang, *Nano Energy*, 2017, **42**, 138-142.
49. Y. Yuan, H. Zhang, J. Wang, Y. Xie, S. A. Khan, L. Jin, Z. Yan, L. Huang, T. Pan and W. Yang, *Materials Research Express*, 2018.
50. X. Wang, S. Niu, Y. Yin, F. Yi, Z. You and Z. L. Wang, *Advanced Energy Materials*, 2015, **5**.
51. J. Chen, J. Yang, Z. Li, X. Fan, Y. Zi, Q. Jing, H. Guo, Z. Wen, K. C. Pradel and S. Niu, *ACS nano*, 2015, **9**, 3324-3331.
52. Y. Yang, H. Zhang, Z.-H. Lin, Y. S. Zhou, Q. Jing, Y. Su, J. Yang, J. Chen, C. Hu and Z. L. Wang, *ACS nano*, 2013, **7**, 9213-9222.
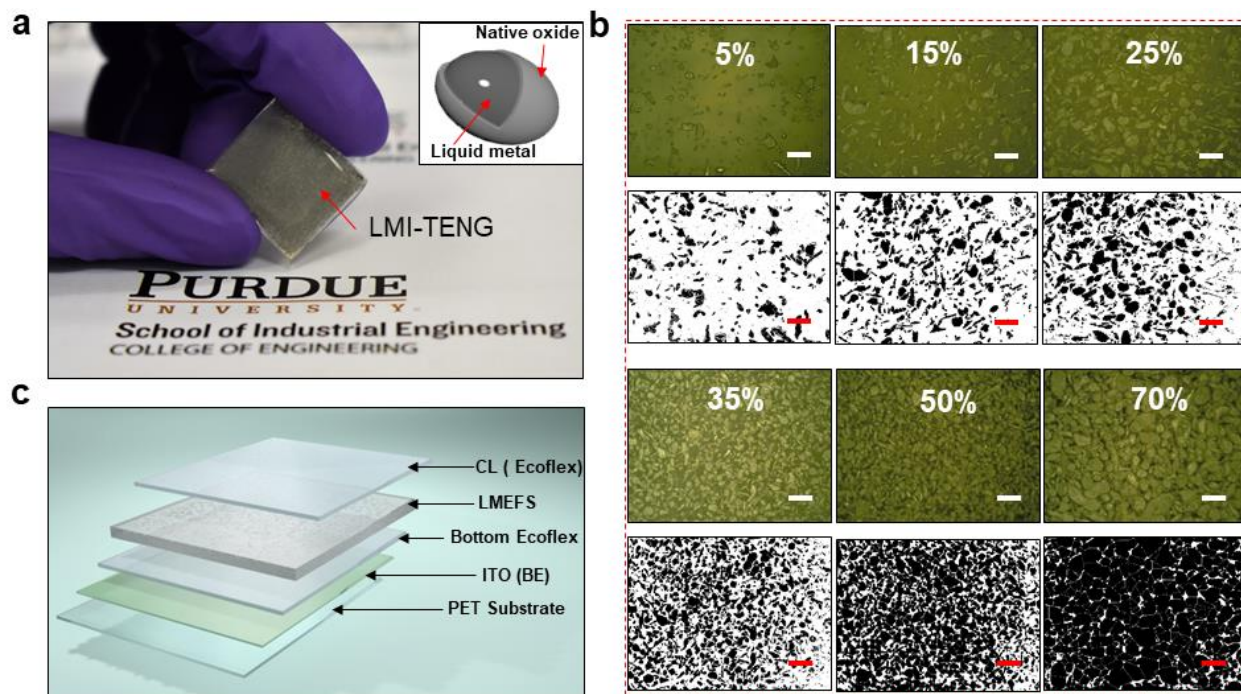
**Figures**



**Figure 1 Design of LMI-TENG. | (a)** The optical image of LMI-TENG. Inset: Schematic illustration of the microstructure of the liquid metal particle (LMP). **(b)** Top-down optical and processed images of the distribution of different wt.% LMPs inside the silicone matrix. **(c)** 3D Schematic illustration of LMI-TENG's structure.
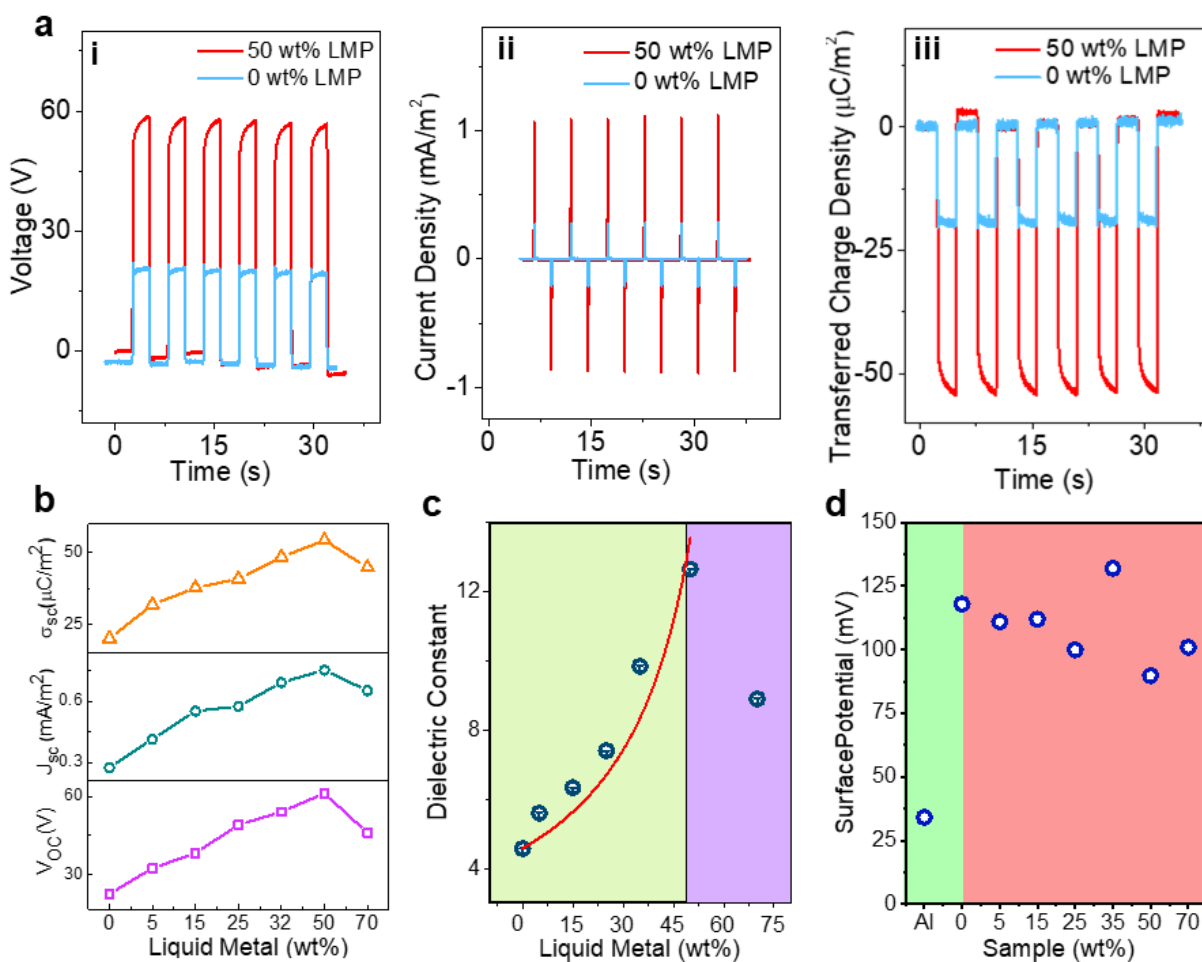
**Figure 2 Electrical Characterization of LMI-TENG. | (a)** The comparison between 0 wt.% and 50 wt.% LMI-TENG's open-circuit voltage (i), short-circuit current density (ii) and short-circuit transferred charge density (iii). **(b)** Working performance summary of LMI-TENG with different wt.% of liquid metal. **(c)** The relationship between the dielectric constant of SDS and weight fraction of LMPs. **(d)** The surface potential of the contact layer on different types of SDS measured by KPFM.
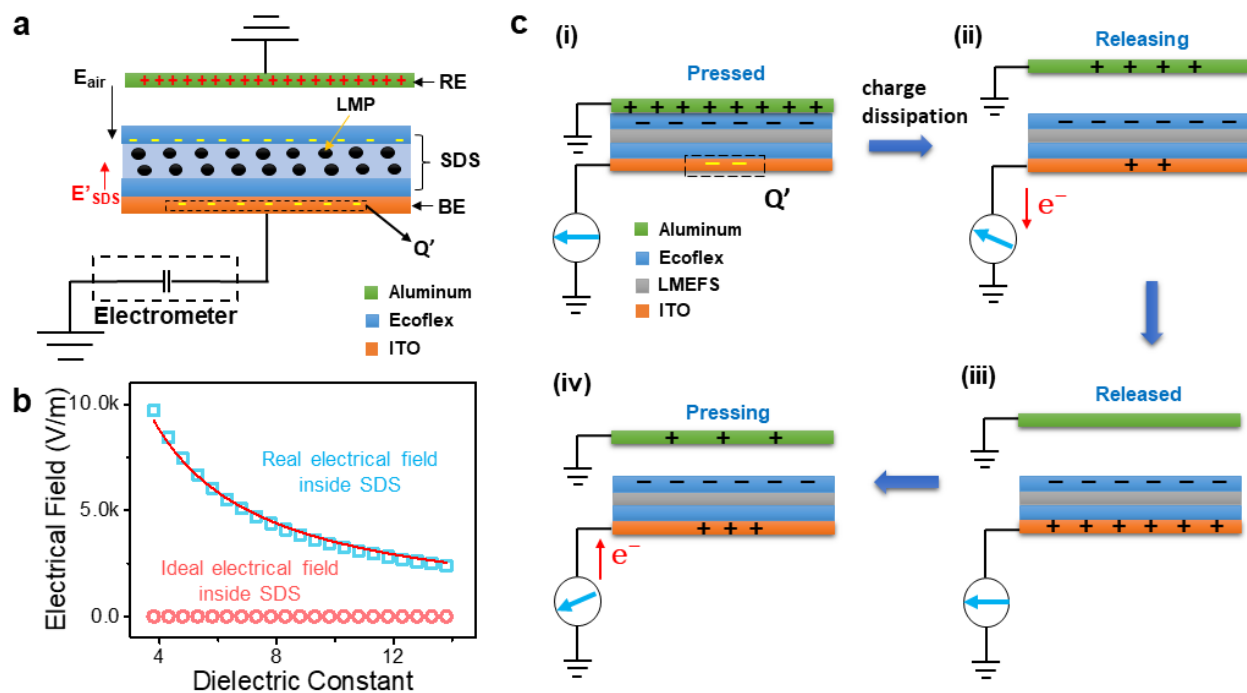
**Figure 3 Electrostatic interaction in LMI-TENG considering the effect of surface leakage charges.** | **(a)** Schematic illustration of the electrostatic induction and charge distribution within SDS and BE. **(b)** FEA result of the electrical field as a function of the dielectric constant in SDS. **(c)** The illustration of the modified TENG working mechanism for LMI-TENG.
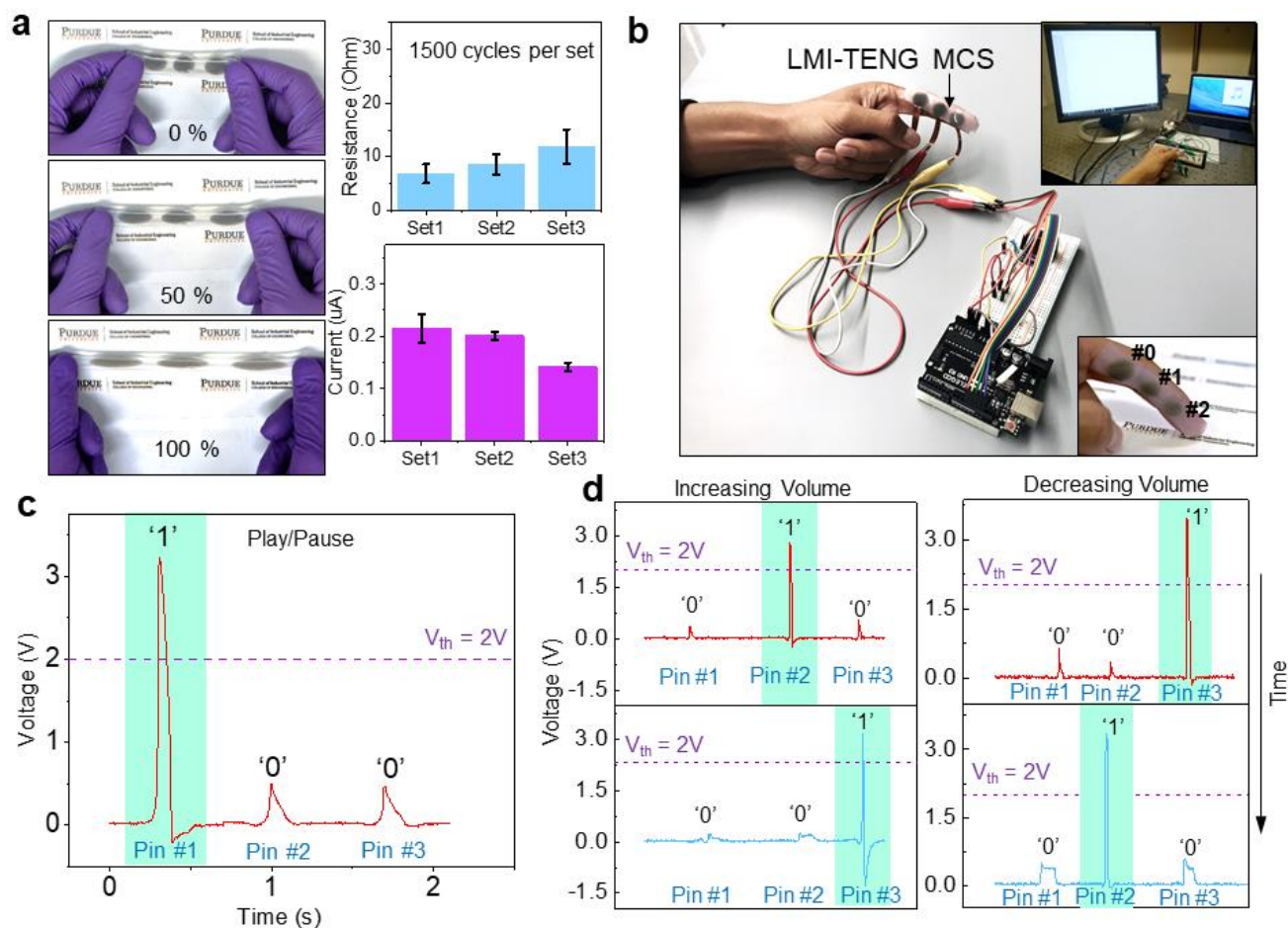
**Figure 4 LMI-TENG for self-powered user interface application. | (a)** The stretchability test of LMI-TENG with Ag NWs electrode. **(b)** Optical image of the wearable LMI-TENG MSC. Inset: the illustration of the testing system and a wearable LMI-TENG MSC device. Detailed operations of the MSC please refer to the supporting video. **(c), (d)** The status signals corresponding to different user interface functions achieved in MCS.